

Causes of Extreme Ridges That Induce California Droughts

HAIYAN TENG AND GRANT BRANSTATOR

National Center for Atmospheric Research,^a Boulder, Colorado

(Manuscript received 14 July 2016, in final form 20 October 2016)

ABSTRACT

California droughts are often caused by high-amplitude and persistent ridges near and off the west coast of North America without apparent connections with ENSO. Here with a hierarchy of climate models, it is demonstrated that extreme ridges in this region are associated with a continuum of zonal wavenumber-5 circumglobal teleconnection patterns that originate from midlatitude atmospheric internal dynamics. Although tropical diabatic heating anomalies are not essential to the formation and maintenance of these wave patterns, certain persistent heating anomalies may double the probability of ridges with amplitudes in the 90th percentile occurring on interannual time scales. Those heating anomalies can be caused by either natural variability or possibly by climate change, and they do not necessarily depend on ENSO. The extreme ridges that occurred during the 2013/14 and 2014/15 winters could be examples of ridges produced by heating anomalies that are not associated with ENSO. This mechanism could provide a source of subseasonal-to-interannual predictability beyond the predictability provided by ENSO.

1. Introduction

The state of California experienced one of the worst droughts in its historical record during 2012–15 (Seager et al. 2015). During the peak phase of the drought, specifically the winters of 2013/14 and 2014/15, the mean atmospheric circulation was dominated by a persistent and high-amplitude ridge near and off the west coast of North America and by a deep trough located to the east of the ridge (Fig. 1). The ridge disrupted the storm track resulting in extremely dry and warm conditions in California, while the trough promoted intense cold snaps across most regions in central and eastern North America (van Oldenborgh et al. 2015; Yu and Zhang 2015). During these two winters the DJF seasonal mean geopotential height at 35°–50°N, 140°–120°W at both 200 and 500 hPa ranked as the top two highest values during the entire record of the NCEP–NCAR reanalyses (Kalnay et al. 1996). Understanding why these ridges and associated wave patterns had such high amplitude and long persistence has motivated us to investigate the mechanisms that produced circulation events like these.

Despite some speculation that the extreme ridges during the recent California drought were likely caused by the warming of the tropical oceans associated with global warming (Palmer 2014; Wang et al. 2014; Swain et al. 2014), more studies have attributed the wave pattern to natural variability of sea surface temperature (SST; Hartmann 2015; Seager et al. 2015; Seager and Henderson 2016; Lee et al. 2015) or of the tropical circulation (Watson et al. 2016). The mechanism associated with SST fluctuations is supported by simulations from multiple atmospheric general circulation models (AGCMs), either with prescribed SST (Hartmann 2015; Seager et al. 2015; Seager and Henderson 2016; Lee et al. 2015) or with the tropical circulation relaxed to the observations (Watson et al. 2016). However, those modeling studies have not yet agreed upon which part of the SST anomalies, whether in the tropical Pacific or in both the tropical and extratropical North Pacific, plays the instrumental role in producing the ridge pattern.

The relevance of the SST forcing mechanism is challenged by the large differences in the anomalous SST patterns in the two winters. Although the two winters are characterized by a similar circulation pattern over and near North America (black contours in Fig. 1), the winter of 2013/14 is close to an ENSO neutral state with a Niño-3.4 SST anomaly of -0.3°C , while the winter of 2014/15 features an emerging El Niño with a Niño-3.4 SST anomaly of 0.7°C (dots in Fig. 1). Differences in the

^a The National Center for Atmospheric Research is sponsored by the National Science Foundation.

Corresponding author e-mail: Haiyan Teng, hteng@ucar.edu

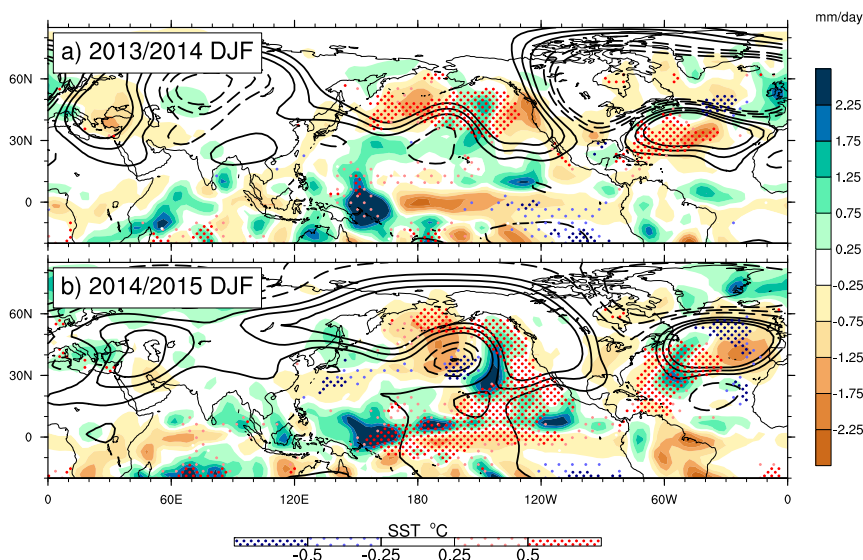


FIG. 1. Seasonal mean z_{200} (contours at ± 20 , 40, and 60 m), precipitation (shading; mm day^{-1}), and SST (dots; $^{\circ}\text{C}$) anomalies in DJF of (a) 2013/14 and (b) 2014/15 relative to the 1979–2015 climatology.

SST anomalies are also pronounced away from the equatorial Pacific Ocean. The SST forcing mechanism was criticized by Baxter and Nigam (2015) for “succumbing to the post-1980–90s temptation of ascribing various extratropical anomalies to ENSO.” Instead, Baxter and Nigam (2015) attributed the 2013/14 circulation pattern to the North Pacific Oscillation–west Pacific pattern (NPO-WP; Linkin and Nigam 2008), which is a combination of extratropical teleconnection patterns rooted in midlatitude dynamics. If this is the correct interpretation, the observed extreme ridge pattern during the 2013/14 winter does not require forcing from the tropics. However, it is intriguing that a similar extreme ridge pattern occurred in two consecutive winters and midlatitude dynamics alone are unlikely to explain such long persistence.

The anomalous circulation patterns during the 2013/14 and 2014/15 winters are just two examples of ridges that caused California droughts. More generally speaking, people have noticed from observations that wet California winters tend to co-occur during El Niño (Jong et al. 2016), but dry California winters are often caused by a ridge off the west coast of North America as part of a midlatitude wave train with no obvious forcing from the tropics (Seager et al. 2015). As elaborated on later in our paper, the possibility that wintertime ridges off the North American west coast do not require tropical forcing for their generation is supported by our analysis of a preindustrial control simulation from the Community Earth System Model, version 1 (CESM1; Kay et al. 2015). When we focus on 500-hPa ridges centered slightly off the

west coast of North America (35° – 50°N , 140° – 120°W), extreme ridges that exceed the 90th-percentile threshold are part of a distinct zonal wavenumber-5 wave pattern in the upper troposphere of the midlatitudes (Fig. 2a) similar to the one documented by Branstator (2002). Occurrences of this wavenumber-5 extreme ridge pattern coincide with stronger rainfall deficits in California but with much weaker tropical precipitation and circulation anomalies compared to composites during extreme ENSO events (Figs. 2b,c), the latter suggesting that the pattern may be an intrinsic mode of the midlatitude atmosphere.

Encouraged by the resemblance between the CESM1 ridge composite pattern (Fig. 2a) and the two observed ridges during the recent California drought (Fig. 1), we undertake a study to investigate the mechanisms that produced west coast ridge events by using simulations from CESM1 together with simulations from a version of CESM1 that does not include ocean coupling, a linear stationary wave model, and reanalysis fields from nature. Our goal has been to determine whether there is merit in the idea that west coast ridges are primarily a manifestation of intrinsic patterns of midlatitude variability that are sometimes excited from the tropics. That west coast ridges do not require tropical forcing anomalies to occur does not rule out the possibility that for some events tropical forcing might be involved. Indeed if they are associated with modes that occur intrinsically, they should be especially easy to excite.

Throughout our study we have been especially interested in extreme events, which we take to be events

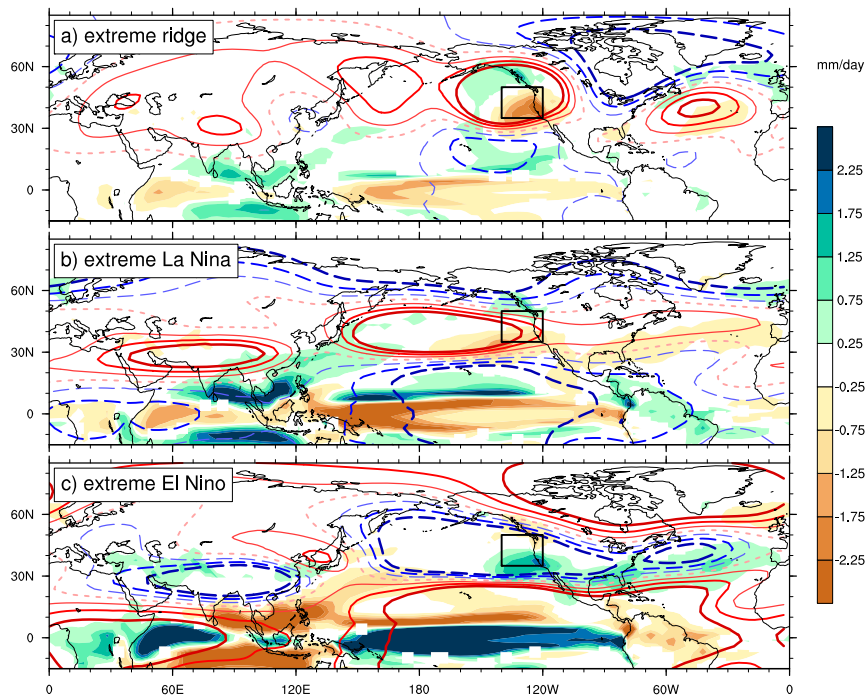


FIG. 2. Composite maps of DJF mean z_{200} (contours at ± 10 , 20, and 30 m with the 0-m contour represented by the red-dashed line) and precipitation (shading; mm day^{-1}) anomalies in the 1800-yr CESM1 preindustrial control simulation for seasons with (a) extreme ridges off the North American west coast (outlined by the box), (b) extreme La Niña, and (c) extreme El Niño. All contours with absolute values larger than 10 m and precipitation anomalies in color-shaded areas are significant at the 90% confidence level.

that occupy the bottom or top 10th percentile of a distribution. (The west coast ridges during the winters of 2013/14 and 2014/15 both satisfy this criterion, with the high pressure anomalies off the west coast of North America ranking as the two highest ridge amplitudes during the 69-yr NCEP–NCAR reanalyses period.)

The models and experiments we have employed are introduced in section 2. In section 3, we demonstrate that there exists a continuum of low-frequency circum-global teleconnection patterns that can produce ridges near the west coast similar to those observed during the peak phase of the recent California drought. These wave patterns can be well captured by a linear stationary wave model, which suggests that the extreme ridge pattern can originate from linear adiabatic dynamical processes in the midlatitudes. In section 4, we further utilize the control simulation from both the fully coupled CESM1 and its atmosphere/land stand-alone components to quantify to what extent tropical forcing can enhance the probability and persistence of the extreme ridges. A summary of our findings is given in section 5, where we conclude that it is indeed useful to think of the extreme ridges being a consequence of two elements: 1) the existence of a continuum of intrinsic midlatitude

circulation patterns that include ridges near the west coast and 2) forcing by tropical heating in special regions that are especially adept at exciting these patterns.

2. Observational data and model simulations

In our investigation, circulation anomalies are diagnosed using the NCEP–NCAR reanalyses from 1948 to 2016 (Kalnay et al. 1996), and SST data for the same period are from the Hadley Centre Sea Ice and Sea Surface Temperature dataset (HadISST; Rayner et al. 2003). The Niño-3.4 SST index, which is constructed from HadISST, is downloaded from NOAA/ESRL’s website (http://www.esrl.noaa.gov/psd/gcos_wgsp/Timeseries/Nino34/). The precipitation data during 1979–2015 were produced by the Global Precipitation Climatology Project (GPCP; Adler et al. 2003). All observational diagnoses are based on monthly mean data, which are regridded to T42 grids, corresponding roughly to a 3° latitude–longitude resolution. Only when we study atmospheric intrinsic variability in section 3, we further remove the 3-month running seasonal mean from the monthly anomalies. In other sections, simple monthly or seasonal mean anomalies during DJF are used. We use

geopotential height and meridional wind at 200 hPa to depict planetary wave activity. To quantify the intensity of the ridge off the west coast of North America, as we will show later in the paper, we define a ridge index based on domain-averaged 500-hPa geopotential height anomalies because this variable is more commonly used by operational forecasts.

CESM1 consists of fully coupled atmosphere, ocean, land, and sea ice models. For the control simulation, the greenhouse gas concentration and other anthropogenic forcings were set to preindustrial levels and the model was integrated for 1800 years. Monthly SST and sea ice concentration mean climatologies were then calculated from the CESM1 integration for years 402–1510. With the external forcings set to the same values used in the CESM1 preindustrial control run, these two mean fields were then used to drive only the atmosphere/land components. This atmosphere/land stand-alone experiment, which is referred to as the CAM5 control run, was run for 2600 years and compared to the fully coupled integration to isolate the impact of atmosphere–ocean coupling. Both the CESM1 and CAM5 control simulations were run at a spatial resolution of roughly 1° for all four components, and we regridded the outputs to T42 grids to reduce the data volume. The CESM1 and CAM5 control simulations are both part of the CESM1 large ensemble project documented by Kay et al. (2015).

To study an even simpler dynamical system, we have employed the linear stationary wave model that is described in the appendix of Branstator (1990, referred to as LINCLIN). It is based on the discretized sigma coordinate primitive equations employed by NCAR's Community Climate Model, version 0 (CCM0; Williamson 1983), which is a much earlier version of CAM5. In LINCLIN, the atmospheric states, which consist of zonal and meridional wind, air temperature, and surface pressure, are divided into a climatological mean basic state and perturbations. The primitive equations are therefore represented in the form $\partial\mathbf{X}/\partial t = -\mathbf{L}\mathbf{X} + \mathbf{R}$, where \mathbf{X} contains the coefficients of all perturbation fields at all levels, t is time, \mathbf{L} is a real matrix, and \mathbf{R} contains the coefficients of the forcing. In our study only steady forcing is considered so the system reduces to $\mathbf{L}\mathbf{X} = \mathbf{R}$.

We have run LINCLIN with a horizontal truncation of R15 at 10 equally spaced vertical levels ($\sigma = 0.05, \dots, 0.95$). The mean states are DJF climatological values from the reanalysis. (Our results are not affected in any important way when we replace the reanalysis climatology with the CESM1 or CAM5 climatology.) The linear model includes damping coefficients for each state variable, which are set to $(2 \text{ days})^{-1}$ in the bottom two levels and $(7 \text{ days})^{-1}$ for the rest of the levels. To learn

about the structure of patterns produced by intrinsic dynamical processes, we have forced LINCLIN with randomly generated steady vorticity sources within mid-to-high latitudes in the Northern Hemisphere. These sources represent the scattering of energy produced by midlatitude nonlinear processes. This was done by generating forcing distributions through random draws from a Gaussian distribution, which are assigned to each grid point at each model level. The nondivergent winds at the $0.25\text{-}\sigma$ level from 1000 LINCLIN solutions, each forced by a different random forcing, were then analyzed in the same manner that we analyze variability in 200-hPa anomalies in the reanalysis, CESM1, and CAM5 datasets.

3. A continuum of circumglobal teleconnection patterns

In this section, we demonstrate that the extreme ridge patterns that can cause California droughts are associated with a continuum of wavenumber-5 circumglobal teleconnection patterns (Branstator 2002; Branstator and Selten 2009; Franzke and Feldstein 2005) that originate from adiabatic processes in the midlatitudes. All analyses in this section are derived from DJF monthly mean anomalies with the 3-month running seasonal mean removed (referred to as subseasonal monthly mean anomalies); removing seasonal means minimizes the influence of slowly varying SST anomalies, thus emphasizing the impact of internal atmospheric processes.

Some aspects of low-frequency planetary wave variability can be described in terms of a class of circumglobal teleconnections (CGT) that appear to exist as a result of the waveguide effect of the mean jet (Branstator 1983; Hoskins and Ambrizzi 1993). These waveguide patterns propagate along latitude circles because they tend to be meridionally confined to the vicinity of the jets owing to the strong meridional gradients of mean absolute vorticity that exist on the flanks of the jets. These patterns are readily revealed by empirical orthogonal functions (EOFs) of meridional wind in the upper troposphere. Following Branstator (2002), we apply EOF analysis to DJF subseasonal monthly anomalies of 200-hPa meridional wind v_{200} in the $10^\circ\text{--}70^\circ\text{N}$ band during 1948–2016. The v_{200} anomalies regressed to the principal components associated with the leading two EOFs (shading in Figs. 3a,b) represent a pair of wavenumber-5 CGT patterns oriented along the mean jet. (The dots denote regions with DJF 200-hPa mean zonal wind u_{200} exceeding 25 m s^{-1} .) Branstator (2002) has noted the first leading EOF of meridional wind v_{EOF1} (Fig. 3a) in particular as a special CGT pattern. It is prominent enough in the upper-troposphere circulation to be embedded in the leading EOF of streamfunction as well as meridional wind.

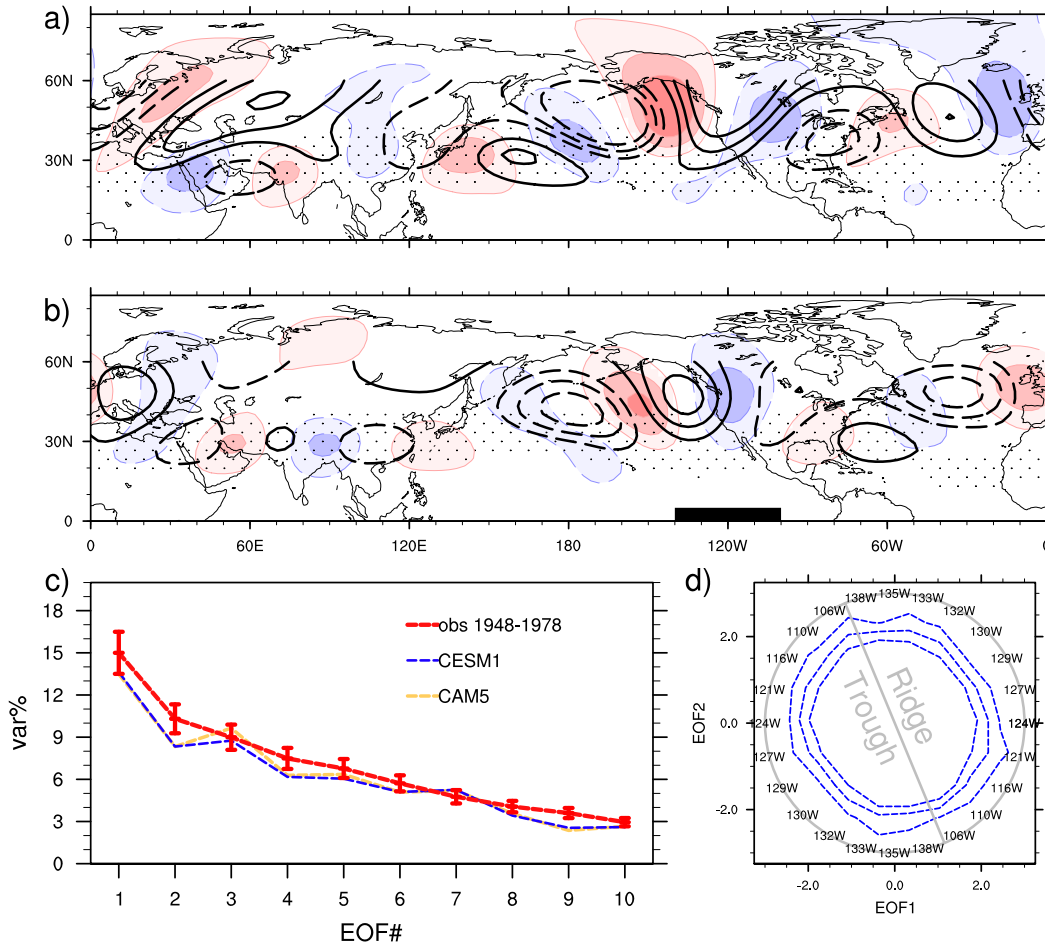


FIG. 3. (a),(b) DJF subseasonal monthly v_{200} (blue and red shading at $\pm 1, 2,$ and 3 m s^{-1}) and z_{200} (black contours at $\pm 10, 20,$ and 30 m) anomalies regressed upon the leading two EOFs of v_{200} at 10° – 70°N during 1948–2015 in the reanalysis (i.e., v_{EOF1} and v_{EOF2}). Stippling denotes regions where the 200-hPa mean jet exceeds 25 m s^{-1} . (c) Percentage of total subseasonal variance in the reanalysis, CAM5 (orange), and CESM1 (blue) explained by the leading 10 meridional wind EOFs in the reanalysis. The error bars are estimated based on North et al. (1982). (d) PDF (contour intervals at 0.5, 1.0, and 1.5) of CESM1 DJF subseasonal monthly v_{200} projections onto v_{EOF1} and v_{EOF2} of the reanalysis [those shown in (a),(b)]. Each angle ($0^{\circ}, 15^{\circ}, 30^{\circ}, \dots, 345^{\circ}$) on the v_{EOF1} – v_{EOF2} plane corresponds to a pattern given by combined v_{EOF1} and v_{EOF2} , which has an associated geopotential trough or ridge in 140° – 100°W (our domain of interest) and is outlined by the thick black line in Fig. 3b. Those longitude values are labeled around the gray circle.

The geopotential height anomalous patterns associated with the leading two meridional wind EOFs are similar at 200 and 500 hPa (z_{200} and z_{500} , respectively). For clarity, we only plot z_{200} anomalies, as derived from regression, south of 60°N (the black contours in Figs. 3a,b). Over the Pacific–North American sector, the z_{200} anomalies for v_{EOF1} are characterized by a wave train with three centers of action in the northern Pacific Ocean, the northwestern sector of North America, and the southeastern United States. To a certain degree, it resembles the Pacific–North American (PNA) teleconnection pattern (Wallace and Gutzler 1981) during a negative phase, which corresponds to negative height anomalies over the northern Pacific Ocean (45°N ,

165°W) and the U.S. Gulf Coast region (30°N , 85°W) and positive anomalies over western Canada (55°N , 115°W) according to Wallace and Gutzler (1981). But compared to the definition of the PNA in Wallace and Gutzler (1981), the v_{EOF1} regressed z_{200} anomalies in Fig. 3a exhibit a wave path with less meridional arching, indicated by the absence of the PNA’s tropical center of action near Hawaii (20°N , 160°W) and small meridional displacements of the two centers of action over North America. The discrepancies may be caused by our emphasis on internal variability with the seasonal mean removed and by an analysis that is based on meridional wind anomalies. Along the jet, the z_{200} anomalies associated with the second leading EOF of meridional wind

v_{EOF2} correspond to a wave pattern similar to those associated with v_{EOF1} but with all centers of action shifted westward by approximately 15° – 20° longitude. We note that the displacement of a ridge on the west coast of North America and subtropical North Atlantic Ocean and an extended trough over northeastern North America and the North Atlantic Ocean resembles the circulation anomalies in the winters of 2013/14 and 2014/15.

Percentage variance explained by the leading meridional wind EOFs and error bars (North et al. 1982) is presented in Fig. 3c. Although v_{EOF1} is distinct from v_{EOF2} , the error bars of v_{EOF2} overlap those for the third leading EOF of meridional wind v_{EOF3} , with the latter corresponding to a zonal wavenumber-6 pattern. From v_{EOF2} to the tenth leading EOF of meridional wind v_{EOF10} , the percentage variance explained decreases more gradually compared to the rather abrupt drop from that of v_{EOF1} to v_{EOF2} , and the error bars associated with v_{EOF2} – v_{EOF10} often overlap with each other. When we project the v_{200} anomalies in CAM5 and CESM1 onto the observed meridional wind EOFs, we find similar variance values in the models. Overall, it seems that except for v_{EOF1} , there exists a collection of wavenumber-5 or wavenumber-6 orthogonal patterns that generally lack distinction in terms of variance represented.

Figure 3 indicates that both v_{EOF1} and v_{EOF2} during the positive phase are associated with ridges off the west coast though centered at different longitudes. Moreover, combinations of these patterns will also produce ridges at still other longitudes off the west coast. And when we have examined the projections onto these two patterns in CESM1, whose abundant data make it possible to depict these states in terms of a joint probability distribution function (PDF) of subseasonal v_{200} in the v_{EOF1} – v_{EOF2} plane (Fig. 3d), we have found that there is no preference for the location of the ridges they have produced. In Fig. 3d, each angle θ on the v_{EOF1} – v_{EOF2} plane corresponds to a pattern, given by $v_{\theta} = v_{\text{EOF1}} \cos(\theta) + v_{\text{EOF2}} \sin(\theta)$, that has an associated geopotential trough or ridge in 140° – 100° W, which is our domain of interest. We estimate the longitude of that feature (labeled around a circle in Fig. 3d) by finding the longitude in that range for which the average of v_{θ} between 30° and 50° N equals zero. The near-circular shape of the PDF (blue contours in Fig. 3d) implies that v_{EOF1} , v_{EOF2} , and any possible linear combinations of the two patterns all have a similar probability of occurrence. There is no indication of clusters of higher-probability ridges occurring at certain longitudes. This is consistent with the finding of Berner and Branstator (2007), though some have argued that such clustering may occur in the atmosphere because of its nonlinearities (Corti et al. 1999).

Combining the variance and PDF results, we conclude that there is a continuum of low-frequency zonal wavenumber-5 patterns that can lead to a ridge or trough near and off the west coast. The extreme ridges in the winters of 2013/14 and 2014/15 are two examples of the collection. In fact, some of the other meridional wind EOFs are also associated with west coast ridges though with somewhat smaller zonal scales, so the collection of patterns that produces such ridges is even larger than the collection produced by v_{EOF1} and v_{EOF2} .

To describe patterns leading to a ridge near and off the west coast, we employ a series of one-point regression maps. First, we regress subseasonal monthly reanalysis v_{200} (blue and red contours), z_{200} (black contours), and precipitation (shading) anomalies upon an index derived by averaging v_{200} anomalies within the domain 40° – 50° N, 95° – 105° W and plot them with signs reversed (box 1; Fig. 4a). This particular reference point is selected for its proximity to one of the centers of action in v_{EOF1} (Fig. 3a). Because of the large variance explained by v_{EOF1} , there is a close resemblance in the spatial structure of the regressed v_{200} and z_{200} anomalies in Figs. 4a and 3a.

We then apply the same regression analysis to the CESM1 (Fig. 4b) and CAM5 simulations (Fig. 4c). The v_{200} anomalies are slightly stronger along the Asian jet in the models than in the reanalysis dataset and constitute a wavenumber-5 CGT pattern similar to v_{EOF1} (Fig. 3a). Over North America and the adjacent oceans the v_{200} and z_{200} anomalies roughly match the corresponding reanalysis plot in Fig. 3a, confirming that v_{EOF1} represents not only more variance than other EOFs but also a dynamical mode of variability. The similarity between the CAM5 fields and the fields for CESM1 and nature is consistent with the PNA being an atmospheric intrinsic mode of variability that does not rely on air–sea coupling (Lau 1981). We can further simplify the dynamical system by considering the LINCLIN solutions described in section 2 for a case when the steady random vorticity forcing is confined to 30° – 90° N. We apply the same regression analysis to meridional wind anomalies at $\sigma = 0.25$ (Fig. 4d), and we find that the resulting v_{200} pattern resembles the patterns in observations, CESM1, and CAM5.

We can get the full continuum of ridge patterns by moving the reference box longitudinally to different positions. Here we only show two examples of shifting the reference box 10° of longitude westward (labeled as box 2) and eastward (labeled as box 3). The regression maps that are produced are shown in Figs. 5 and 6, respectively. For both reference boxes, not only is there a clear resemblance in the regressed v_{200} and z_{200} anomalies in the four dynamical systems, but the regressed v_{200} pattern explains a similar fraction of variance of v_{200}

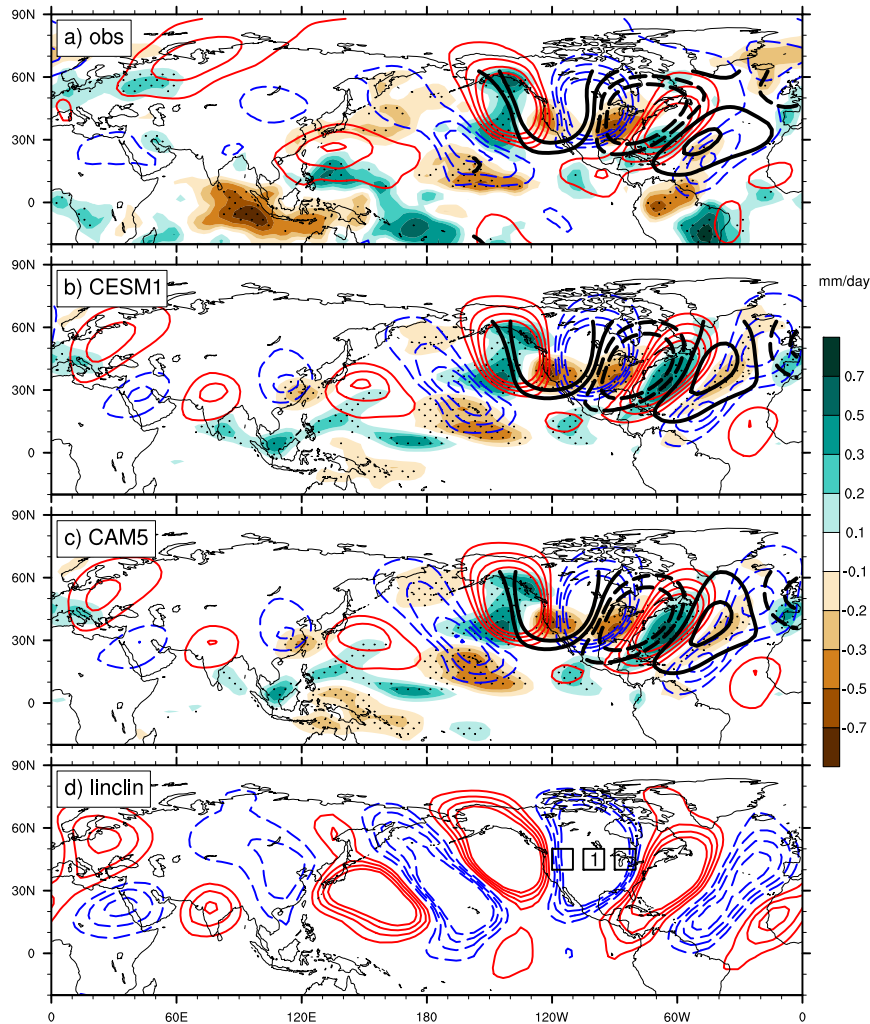


FIG. 4. DJF subseasonal v_{200} (red and blue contours at ± 0.5 , 1, 1.5, and 2 m s^{-1}), z_{200} (black contours at ± 5 and 15 m), and precipitation (shading) anomalies regressed upon domain-averaged subseasonal v_{200} anomalies, with the sign reversed, at box 1 (40° – 50° N, 105° – 95° W) in (a) reanalysis during 1979–2015, (b) CESM1, (c) CAM5, and (d) LINCLIN. Stippling represents the 95% confidence level for regressed precipitation anomalies over the shaded area. The z_{200} anomalies are only plotted over North America and adjacent regions for clarity.

($\sim 10\%$ – 15%) in the reanalysis, CAM5, and CESM1. Note also that the regressed z_{200} anomalies for box 2, in particular, exhibit a spatial structure similar to the 2013/14 and 2014/15 anomalous patterns. The patterns in Figs. 4d, 5d, and 6d are not sensitive to the damping coefficients we use in LINCLIN, but the variance explained by these patterns does show some sensitivity. But with values between 10% and 20% for damping coefficients in the free atmosphere in the range from $(5 \text{ days})^{-1}$ to $(7 \text{ days})^{-1}$, this sensitivity does not affect our interpretation that a range of ridges is produced off the west coast of North America by processes that are intrinsic to midlatitude dynamics.

We also regress the precipitation anomalies (shading in Figs. 4–6) for the same three v_{200} box indices from the reanalysis, CESM1, and CAM5 datasets. Overall, the model anomalies match the reanalysis in midlatitudes in both spatial patterns and amplitude. However, there are large discrepancies in the tropics. For example, the regressed precipitation anomalies in nature for v_{200} in box 1 exhibit a zonal dipole structure associated with excessive rainfall anomalies over the western tropical Pacific and suppressed rainfall anomalies in the eastern Indian Ocean. This structure resembles the tropical rainfall associated with one phase of the Madden-Julian oscillation (MJO; Madden and Julian 1971).

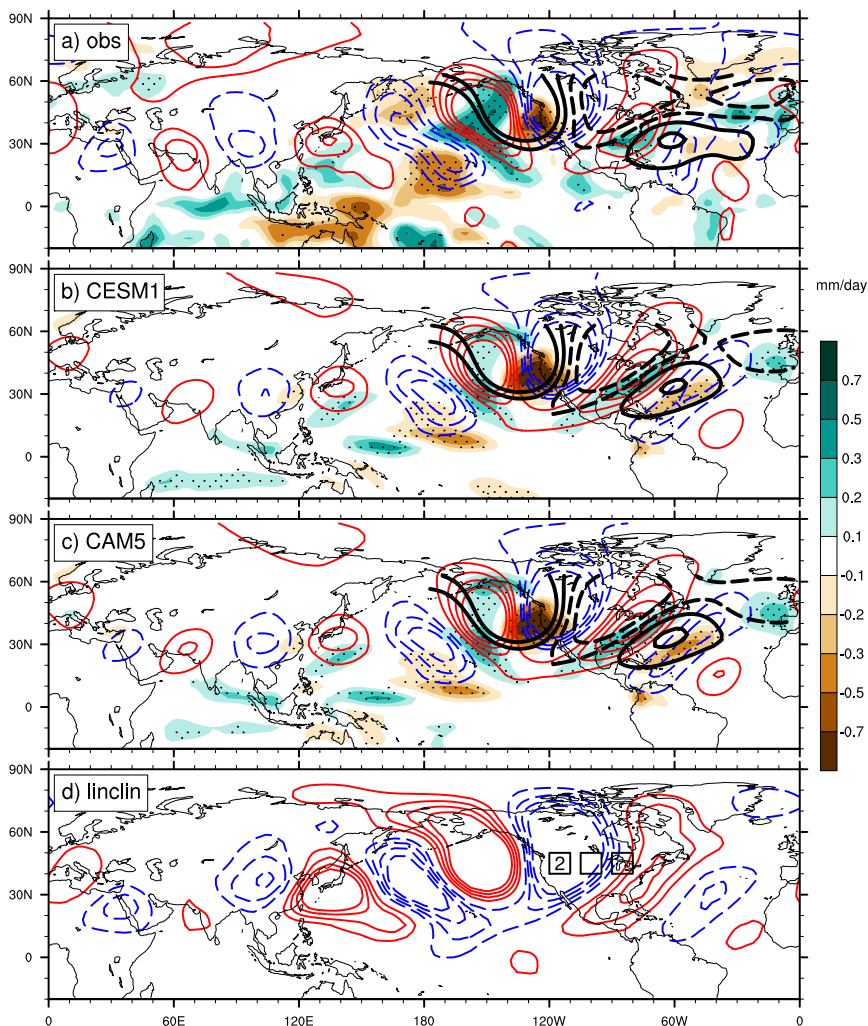


FIG. 5. As in Fig. 4, but for regressed anomalies with respect to domain-averaged v_{200} at box 2 (40° – 50° N, 120° – 110° W).

The regressed precipitation anomalies in the models (Figs. 4b,c) are weaker in amplitude and less spatially organized compared to nature, probably because these models have difficulty simulating the MJO. Similar discrepancies are also obvious in Figs. 5 and 6. The similarity in the wave trains combined with the large discrepancies in tropical precipitation anomalies are consistent with the idea that while tropical precipitation anomalies may induce the midlatitude wave patterns, they are not essential for the maintenance of the midlatitude wave patterns.

4. Tropical forcing

Although the findings in the previous section indicate tropical forcing is not essential to formation and maintenance of the wave trains associated with extreme ridges near the west coast, one might expect it can affect

the probability and persistence of extreme ridges. Here to consider this mechanism we focus on ridges centered at 35° – 50° N, 140° – 120° W (outlined in Fig. 2) and define a ridge index as the average anomalous z_{500} in that region. The extreme ridges in CESM1 in Fig. 2a are selected based on the same index.

a. Monthly and seasonal means

First, we examine the ridge index using DJF monthly data. Note that hereafter we retain the seasonal mean component in the monthly anomalies. We remove the seasonal mean anomalies in the previous section, owing to our interests in atmospheric internal variability. In this section, we keep the seasonal means so that we can estimate how tropical forcing associated with ENSO or anomalous tropical convection can affect the monthly or seasonal mean ridge off the west coast. When we

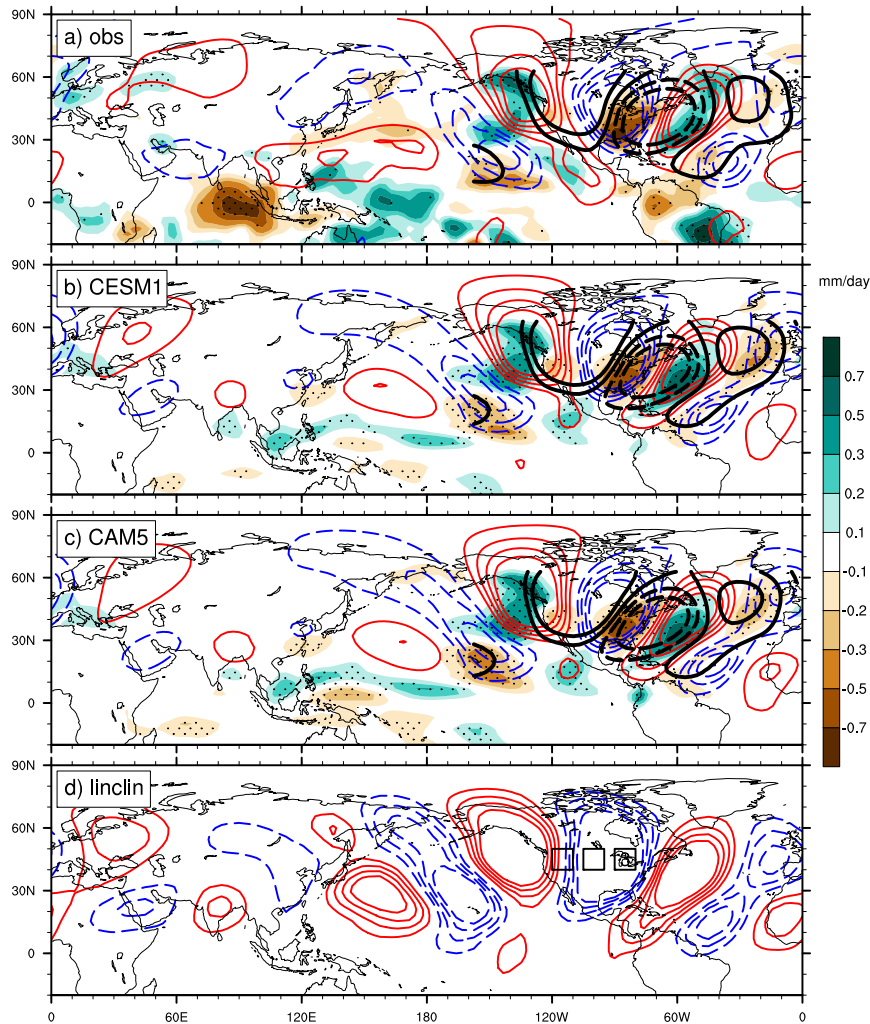


FIG. 6. As in Fig. 4, but for regressed anomalies with respect to domain-averaged v_{200} at box 3 (40° – 50° N, 90° – 80° W).

generate scatterplots of the Niño-3.4 index versus the ridge index for observations (Fig. 7a) and CESM1 (Fig. 7b), the ridge index tends to be negative when the monthly Niño-3.4 SST index is extremely warm, but there is no clear preference for ridges or troughs during months with extreme cold Niño-3.4 SST anomalies. Overall the Niño-3.4 index only explains 5% and 8%, respectively, of the interannual variance in the ridge index in observations and CESM1. With more samples in CESM1, we can also determine the impact of ENSO events on the probability of an extreme ridge or trough off the west coast. Compared to the unconditional probability P_0 (which is 10% because we choose the 90th percentile as the threshold for extremes), the probability of an extreme trough during extreme El Niño winters P_1 (conditional probability of extreme ridge or trough under given condition) almost triples to 29%, while the

probability of an extreme ridge drops to 2%. However, the conditional probability of an extreme ridge during extreme La Niña winters is 13%, only 3 percentage points higher than P_0 .

In addition to ENSO variability, there could be tropical convection not directly associated with ENSO that may contribute to the formation of California drought-causing ridges. To test this possibility, we take a similar approach as above, which is to compare conditional probability (i.e., P_1) with unconditional probability (i.e., P_0), except that the Niño-3.4 index is replaced with local precipitation anomalies in $5^{\circ} \times 5^{\circ}$ latitude–longitude boxes over the tropical ocean. We then plot at each box location the percentage change in probability in the form $100(P_1 - P_0)/P_0$ for both CAM5 and CESM1 (Figs. 8a,c). To further simplify our results, we mainly focus on precipitation anomalies in the tropical Pacific

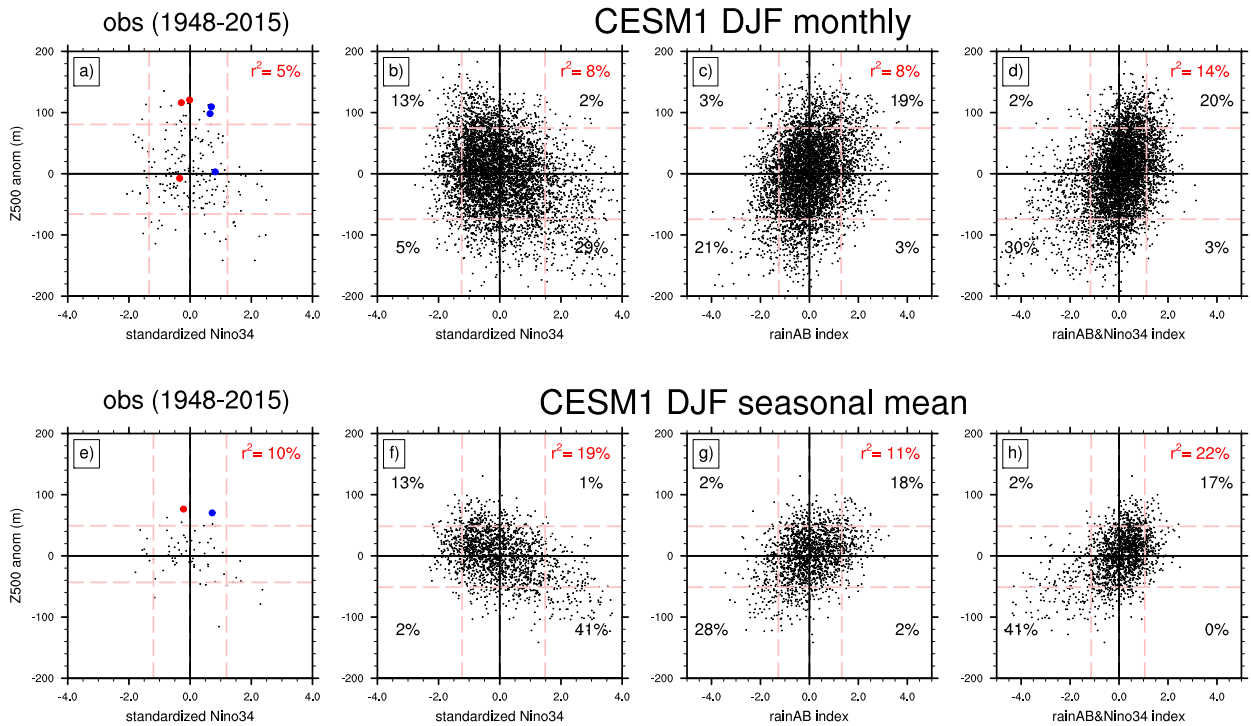


FIG. 7. Scatterplot of DJF (a)–(d) monthly and (e)–(h) seasonal mean ridge index vs Niño-3.4 SST anomalies in (a),(e) observations during 1948–2015 and (b),(f) CESM1. (c),(d),(g),(h) As in (b),(f), but for replacement of the x axis with (c),(g) the rain_{AB} index and (d),(h) the combined Niño-3.4 SST and rain_{AB} index. The squared correlation coefficient is noted in the upper-right corner of each panel. The black number in all four corners of each panel represents the conditional probability of extreme ridges (troughs) (with the threshold values indicated by the red horizontal dashed lines) when the x axis is below (above) the 10th (90th)-percentile threshold (indicated by the red vertical dashed lines). The red and blue dots in (a),(e) denote values for winters of 2013/14 and 2014/15, respectively.

Ocean because we find the associated diabatic heating anomalies in the Pacific are more effective in forcing ridges near the west coast than those in the Indian and the Atlantic Ocean. We also avoid the eastern Pacific off the Baja Peninsula because the region is close to California, making it difficult to distinguish cause and effect.

Figures 8a and 8c reveal multiple locations where extremely high rainfall may increase or decrease the probability of an extreme west coast ridge by more than 50% in the simulations. In the fully coupled run (Fig. 8c), the largest region where extreme precipitation may significantly reduce or enhance the probability of extreme ridges and troughs is located in the equatorial Pacific Ocean, where percentage changes from P_0 to P_1 are consistent with our earlier estimate based on the Niño-3.4 SST index (Fig. 7b). This equatorial Pacific pattern is the major difference between the CESM1 and CAM5 results. Other than that, both the CESM1 and CAM5 simulation indicate extreme precipitation in the equatorial western Pacific (0° – 10° N, 140° – 170° E; labeled as A in Fig. 8) and in the northwestern subtropical Pacific (20° – 30° N, 135° – 155° E; labeled as B in Fig. 8) may enhance the probability of extreme ridges by more than 50%.

Next we form an index that combines the effect of A and B rainfall. This index results from applying multivariate regression to predict the ridge index from A and B rainfall. The index, referred to as rain_{AB} , is expressed as $\text{rain}_{AB} = 8.6\text{Rain}_A + 13.8\text{Rain}_B - 0.03$, where Rain_A and Rain_B represent standardized precipitation anomalies in domains A and B , respectively. The purpose of this statistical model is to provide an optimistic estimate of how much diabatic heating anomalies associated with tropical convection at these two special locations can affect the probability of the ridge. A scatterplot of the rain_{AB} index versus the ridge index for CESM1 data is displayed in Fig. 7c. The rain_{AB} index explains 8% of the variance of the ridge index. Furthermore, when the rain_{AB} index exceeds its 90th percentile, 20% of those months have an extreme ridge, suggesting that certain tropical heating patterns can double the chance of an extreme ridge.

To show how much additional information rainfall anomalies in domains A and B add to the Niño-3.4 index in explaining the variability of the ridge and the probability of extreme ridges, we use multivariate regression to construct another index based on standardized Rain_A ,

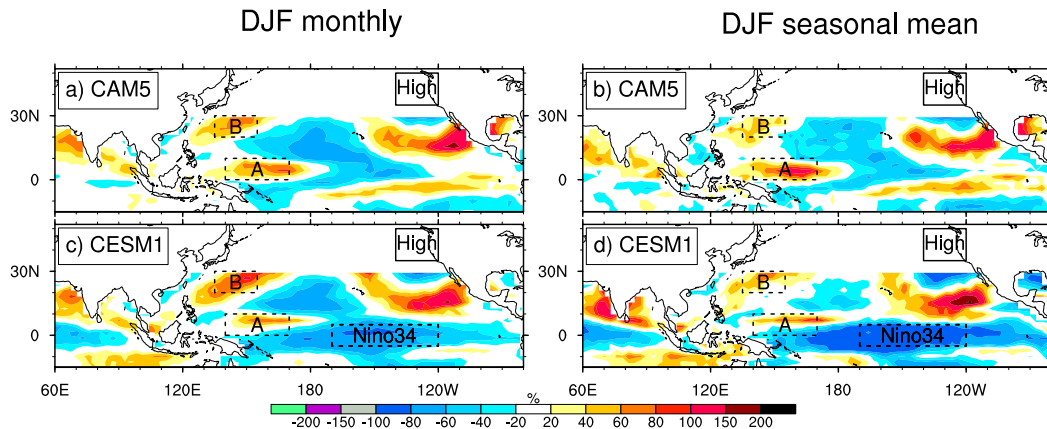


FIG. 8. Percentage change in the probability of extreme ridges at 35° – 50° N, 140° – 120° W (outlined by the box labeled “High”) from $P_0 = 10\%$ to P_1 upon extreme local precipitation at any $5^{\circ} \times 5^{\circ}$ latitude–longitude boxes over the tropical ocean, in the form $100(P_1 - P_0)/P_0$ for (a),(b) CAM5 and (c),(d) CESM1. (left) Extreme DJF monthly ridges and (right) extreme seasonal ridges.

Rain_B , and Niño-3.4 SST anomalies: $\text{rain}'_{AB} = 11.2\text{Rain}_A + 8.2\text{Rain}_B - 15.7(\text{Niño-3.4 SST}) - 0.03$. The scatterplot of the ridge versus this three-variable index is shown in Fig. 7d. This new index can explain 14% of the ridge variability, compared to 8% by either Niño-3.4 SST (Fig. 7b) or the rain_{AB} index alone (Fig. 7c). When the index exceeds the 90th percentile, it doubles the probability of the extreme ridge, similar to the rain_{AB} index.

To demonstrate how tropical heating anomalies represented by rain_{AB} may affect the midlatitude circulation throughout the Northern Hemisphere, we construct composite maps of z_{200} and precipitation anomalies for winter months with the rain_{AB} index exceeding its 90th-percentile threshold (Fig. 9a). The z_{200} anomalies (Fig. 9a) exhibit a zonal wavenumber-5 CGT pattern, which resembles the composite map of the CESM1 extreme ridges (Fig. 2a).

We can further improve this rainfall and Niño-3.4 SST combined index by including more information about tropical heating anomalies represented by rainfall anomalies. One test we have done is to replace Rain_A and Rain_B with the leading EOFs of tropical precipitation anomalies in the Pacific and Indian Oceans. By including different numbers of EOFs, or by changing the domain of the EOF analysis, we find that in some cases when the resulting indices exceed the 90th percentile, the probability of an extreme ridge is doubled or even tripled. Note that these associations between tropical heating and west coast ridges only give an upper limit on the potential for tropical heating to cause ridges. After all, this analysis does not sort out cause and effect. Furthermore, we have not checked the robustness of the results through cross validation. Since we find that even in our best cases extreme ridges occur less than 30% of the time that the tropical index exceeds its extreme threshold, though

tropical heating can affect the likelihood of an extreme ridge, whether an extreme ridge will occur is likely largely determined by midlatitude internal dynamics rather than by the tropical forcing.

As we mentioned, the statistical models above can only provide suggestions as to where tropical heating can potentially affect the probability of west coast ridges. To investigate whether heating locations A and B can definitely cause such ridges we impose heating anomalies at these locations in the linear stationary wave model so that cause and effect are well defined. In these experiments the heating anomalies are placed in elliptical regions that have 1500-km semimajor axes in the longitudinal direction and 1000-km semiminor axes in the latitudinal direction. In the vertical, the heating has the profile $\sin(\pi p/p_s)$, where p and p_s represent pressure level and surface pressure, respectively. The heating anomaly averaged over the entire region, both horizontally and vertically, is $2.5^{\circ}\text{C day}^{-1}$, corresponding to about 2 mm day^{-1} precipitation anomalies.

The LINCLIN response in streamfunction at $\sigma = 0.55$ to the specified heating anomaly in domains A and B is shown in Figs. 10b and 10c, respectively. For comparison, we plot the extreme ridge composite map of 500-hPa streamfunction Ψ_{500} in Fig. 10a. Individually, the heating anomalies in both domains do force anticyclonic circulation anomalies off or near the west coast. In addition, the forced streamfunction anomalies in both cases project onto the wavenumber-5 CGT pattern that extreme ridges are associated with (Fig. 10a).

We have repeated the above data analyses with DJF seasonal mean anomalies, and the results are shown in Figs. 7 (bottom) and 9 (bottom) and Fig. 8 (right). Consistent with the analysis based on monthly data, extreme seasonal rain_{AB} may approximately double the

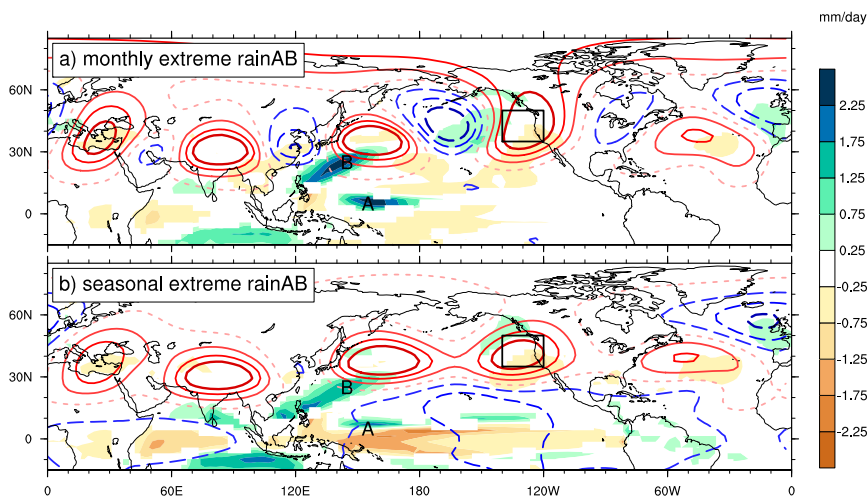


FIG. 9. CESM1 composite maps of DJF (a) monthly and (b) seasonal mean z_{200} (contours at ± 10 , 20, and 30 m with the 0-m contour represented by the red-dashed line) and precipitation (shading) anomalies for months or seasons with the rain_{AB} index exceeding the 90th-percentile threshold. The two locations from which the rain_{AB} index is constructed are labeled as A and B, and the domain of the ridge index is outlined by the box.

probability of seasonal extreme ridges (Fig. 7g). In addition, the seasonal rain_{AB} extremes are associated with stronger negative convection and z_{200} anomalies in the equatorial Pacific compared with the monthly rain_{AB} extremes (Fig. 9). This possibly results from CESM1 rainfall anomalies in domains A and B being caused to a certain degree by ENSO, especially on seasonal time scales. This possibility is supported by a comparison of the PDF of Niño-3.4 SST anomalies for months and seasons with extreme rain_{AB} (Fig. 11). While the PDF of months with extreme rain_{AB} (blue line) exhibits only a small shift toward La Niña compared with that of all monthly data (black solid line), there is a much bigger shift in the Niño-3.4 PDF during seasonal rain_{AB} extremes (red). Despite the preference of extreme rain_{AB} occurring during La Niña winters, Fig. 11 also indicates that in CESM1 many extreme rain_{AB} cases, on both monthly and seasonal time scales, take place during ENSO neutral or even warm phases.

b. 2-yr ridges

One key trait of the recent California drought is that a similar extreme ridge pattern predominated in two consecutive winters. When we investigate the probability of 2-yr extreme ridges, we find that their probability of occurrence is only 0.77% in CAM5; this probability of occurrence is boosted to 1.33% in CESM1 via low-frequency air-sea coupled variability such as ENSO. Nevertheless, the chance for 2-yr extreme ridges is very low, and we find only 23 such events in the 1800-yr CESM1 run.

To reveal the spatial distribution of SST anomalies before and during two-year extreme ridges in CESM1, we construct composite maps of the 23 two-year extreme ridge events in CESM1. Here year 0 is defined as the first year when the seasonal mean ridge index exceeds the 90th-percentile threshold. SST anomalies in year -1 , year 0, and year 1 are shown as stippling in Fig. 12, while the z_{200} and precipitation anomalies are superimposed as contours and shading, respectively. While there are almost no significant precursor SST anomalies for DJF in year -1 , the equatorial Pacific is characterized by having a weak La Niña in both year 0 and year 1. The averaged Niño-3.4 SST anomaly is -0.26°C and -0.43°C , respectively. Out of the total 23 cases, six have Niño-3.4 SST anomalies colder than -0.5°C in DJF of both year 0 and year 1, confirming that 2-yr La Niña events (Okumura and Deser 2010) play an important role in some persistent extreme ridge events, but they are not a necessary condition (as five cases have Niño-3.4 SST anomalies greater than 0.5°C in year 0 and one case has a Niño-3.4 value greater than 0.5°C in year 1). The lack of precursor SST anomalies in year -1 (Fig. 12a) and lack of a coherent evolution of the Niño-3.4 SST anomalies in the 23 cases both indicate that 2-yr extreme ridges are not necessarily an ENSO precursor mode in this model as suggested by Yoon et al. (2015).

While the composite maps (Fig. 12) hint that rainfall anomalies at A and B may potentially increase the probability of 2-yr extreme ridges, it is difficult to quantify this effect with only 23 events in CESM1. To expand the sample size, we use the 75th percentile as the

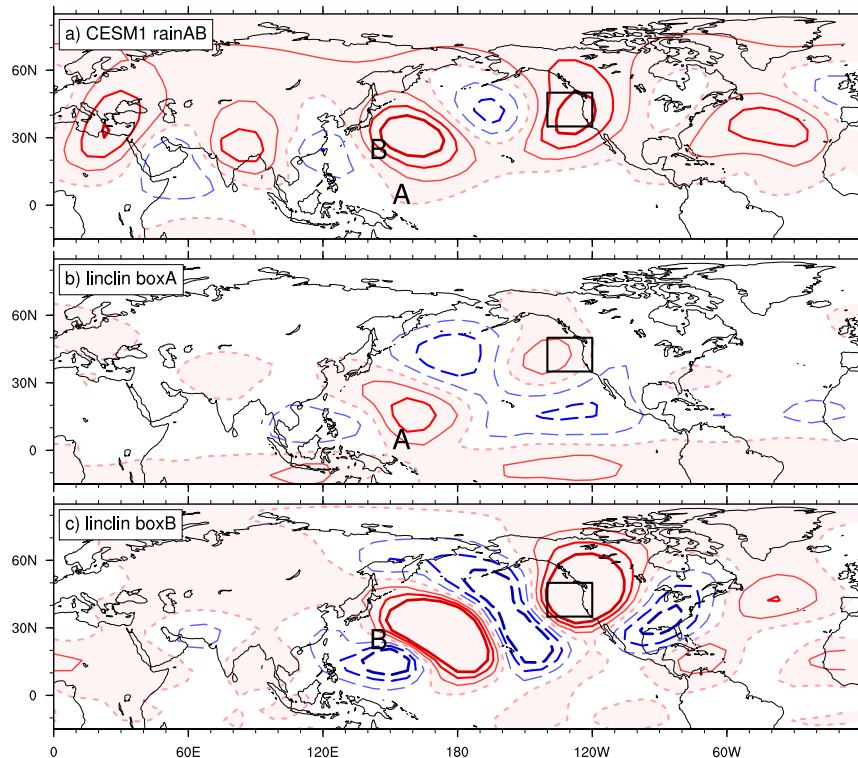


FIG. 10. (a) CESM1 composite maps of DJF monthly Ψ_{500} anomalies ($\pm 1 \times 10^6$, 2×10^6 , and $3 \times 10^6 \text{ m}^2 \text{ s}^{-1}$) for months with the rain_{AB} index exceeding the 90th-percentile threshold. LINCLIN response in streamfunction at $\sigma = 0.55$ to specified heating of $2.5^\circ\text{C day}^{-1}$ at (b) box A (5°N , 155°E) and (c) box B (25°N , 145°E). Shading in light red color highlights areas with positive anomalies, and the domain of the ridge index is outlined by the box.

threshold and find 135 events with 2-yr moderate ridges ($P_0 = 7.5\%$). In addition, out of the total 119 events when the seasonal rain_{AB} index exceeds the 75th percentile in two consecutive winters, 22 correspond to 2-yr moderate ridge events ($P_1 = 18.5\%$). Thus, moderate heating anomalies at A and B may make 2-yr moderate ridges twice as likely to occur.

Given the infrequent occurrence of 2-yr extreme ridges in CESM1, it is tempting to attribute the observed 2-yr extreme ridges during the recent California drought to climate change rather than natural variability. When we have examined the circulation trend of CESM1 in a twenty-first-century climate change projection forced by RCP8.5 (Kay et al. 2015), we have seen no evidence that ridges become more prevalent off the west coast compared with other regions at similar latitudes in the future climate (not shown). But as discussed by Seager et al. (2015), attribution of the extreme ridge pattern to climate change heavily relies on the fidelity of the model-simulated SST response in the equatorial Pacific to anthropogenic forcing. Like many CMIP5 models, the CESM1 climate change projection experiment (Kay et al. 2015) produces stronger warming in the

central and eastern equatorial Pacific than in the western equatorial Pacific (not shown), which deviates substantially from the observed trend (not shown). Thus, within our study's framework we are unable to come to any conclusions regarding the contribution climate change may be making to the likelihood of long-lived west coast ridges.

5. Conclusions

We have investigated the origin of the wave patterns associated with extreme ridges near the west coast of North America, including the extreme ridges that caused the recent California droughts in two consecutive winters. Similar wave patterns can be produced by a hierarchy of climate models, including a fully coupled Earth system model CESM1, its atmosphere/land components (CAM5) forced with the CESM1 climatological SSTs and sea ice, and a $10\text{-}\sigma$ -level linearized primitive equation model. The presence of the wave patterns in the latter model makes it clear that linear adiabatic dynamical processes are sufficient to produce the ridges and the wave patterns that accompany them.

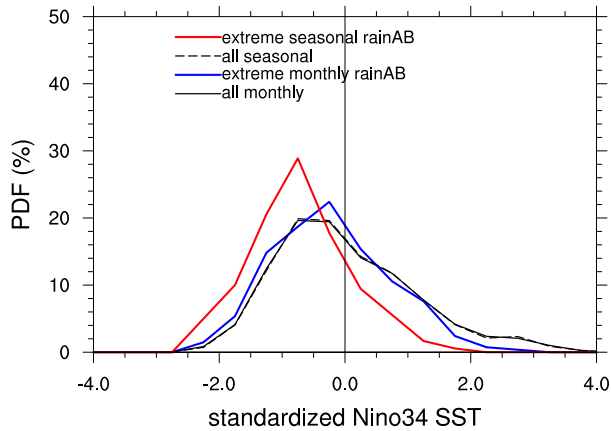


FIG. 11. PDFs of DJF monthly (blue) and seasonal mean (red) Niño-3.4 SST anomalies for months or seasons with the rain_{AB} index exceeding the 90th-percentile threshold in CESM1. The black solid and dashed lines represent the PDF for all monthly and seasonal mean Niño-3.4 SST anomalies in the CESM1 run, respectively.

Our findings indicate that the intrinsic patterns that are associated with west coast ridges are members of a continuum of patterns that are zonally oriented, trapped in the mean tropospheric jet, more or less circumglobal,

and owe their existence to the waveguiding effect of that jet. One phase of each pattern in this continuum includes a ridge off the west coast of North America, and one member of this collection is similar in structure to the anomalous circulation patterns associated with the extreme ridges that occurred during the California drought winters of 2013/14 and 2014/15.

The implication that extreme west coast ridges do not rely in any fundamental way on tropical heating anomalies for their existence is similar to the conclusion of [Baxter and Nigam \(2015\)](#) that the extreme ridge pattern that occurred in the 2013/14 winter does not necessarily originate directly from tropical heating anomalies. But they argued that the ridge pattern is a manifestation of the NPO-WP pattern, which is characterized by a large-scale meridional dipole structure in sea level pressure and geopotential height over the North Pacific, which we believe is not a close match to the structure of the recent drought pattern while the waveguide patterns are.

Though tropical forcing associated with anomalous SSTs or convection is not essential for formation of these wave patterns, our results show that their probability of occurrence and persistence can be affected by long-lived

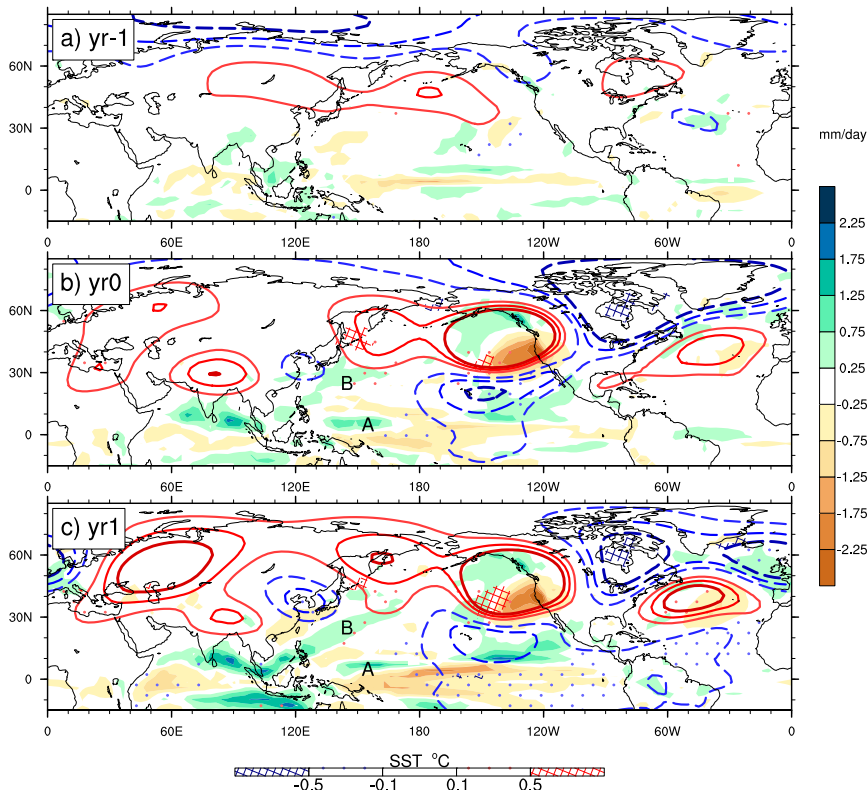


FIG. 12. Composite maps of DJF seasonal mean z_{200} (contours at ± 10 , 20, and 30 m), precipitation (shading), and SST (hatching) anomalies based on 23 cases with 2-yr extreme ridges off the west coast in the 1800-yr CESM1 run. DJF seasonal mean anomalies in (a) year -1 , (b) year 0, and (c) year 1.

tropical heating anomalies, which seems to agree with Seager and Henderson (2016). This finding is consistent with the fact that the natural frequency of the continuum of patterns must be close to zero for them to have occurred prominently in our steady linear planetary wave model experiments. With the CESM1 simulation, we have identified multiple locations in the tropical Pacific where 90th-percentile extreme local precipitation events may increase the probability of 90th-percentile extreme ridges off the west coast by more than 50%. The combined influence from tropical convection anomalies (e.g., those at locations we referred to as domain *A* and *B*) may double the probability of extreme ridges near the west coast during extreme stages of the tropical heating. We have tested more complicated tropical forcing indices by including rainfall information from more locations and ENSO and have failed to produce an index that is associated with more than a 30% chance of an extreme ridge occurring. Therefore, we conclude that, in general, of the two processes that affect the formation of extreme west coast ridges, namely internal midlatitude dynamics and the response to tropical heating, the former makes a larger contribution.

Though we believe this conclusion is not affected by errors in the models we have analyzed, it is best to keep in mind that various model errors may affect some of our quantitative results. For example, our measure of the extent to which tropical forcing can affect the probability of the extreme ridges and our comparison of the relative potential for ENSO and non-ENSO heating to improve extreme ridge forecasts are likely to be affected by model imperfections. While we believe our quantification is useful, more accurate results would benefit from reduced model errors in 1) ENSO amplitude, spatial structure, and teleconnections; and 2) subseasonal-to-interannual variability of tropical precipitation and its relationship to ENSO. In addition, at the present stage, uncertainty in the CESM1-projected trend in equatorial SST and convection is a major obstacle for attribution of the observed 2-yr extreme ridges to climate change.

Despite these unavoidable shortcomings in the model we have used, we believe the various implications of our work are valid. Perhaps paramount among these is that there are tropical heating anomalies that do not depend on ENSO that may excite extratropical responses (Barsugli and Sardeshmukh 2002; Hoerling and Kumar 2002) that include extreme west coast ridges. This mechanism can provide a source of subseasonal-to-interannual predictability, provided the tropical heating anomalies can persist. Here we only use precipitation anomalies at domain *A* and *B* as examples to demonstrate such an effect. A more thorough scrutiny of locations of tropical heating sources that can most effectively induce

extreme ridges and associated wave patterns could potentially improve future forecasts of California droughts beyond what can currently be achieved, especially during nonmature ENSO phases.

Acknowledgments. We thank Drs. Minfang Ting and Richard Seager for constructive reviews. Outputs from the CESM1 large ensemble project were post-processed by Gary Strand and are available from the Earth System Grid (<http://www.earthsystemgrid.org>). This study was supported by the Regional and Global Climate Modeling (RGCM) program of the U.S. Department of Energy's Office of Science Biological and Environmental Research (BER) Cooperative Agreement DE-FC02-97ER62402 (PI: Gerald A. Meehl) and by National Energy Research Scientific Computing Center, which is supported by the Office of Science of the U.S. Department of Energy under Contract DE-AC02-05CH11231 (PI: Gerald A. Meehl), and by the National Science Foundation. GB acknowledges support by NOAA MAPP NA14OAR4310224 and NASA NEWS via NA09OAR4310187.

REFERENCES

- Adler, R. F., and Coauthors, 2003: The version-2 Global Precipitation Climatology Project (GPCP) monthly precipitation analysis (1979–present). *J. Hydrometeorol.*, **4**, 1147–1167, doi:10.1175/1525-7541(2003)004<1147:TVGPCP>2.0.CO;2.
- Barsugli, J. J., and P. D. Sardeshmukh, 2002: Global atmospheric sensitivity to tropical SST anomalies throughout the Indo-Pacific basin. *J. Climate*, **15**, 3427–3442, doi:10.1175/1520-0442(2002)015<3427:GASTTS>2.0.CO;2.
- Baxter, S., and S. Nigam, 2015: Key role of the North Pacific Oscillation–west Pacific pattern in generating the extreme 2013/14 North American winter. *J. Climate*, **28**, 8109–8117, doi:10.1175/JCLI-D-14-00726.1.
- Berner, J., and G. Branstator, 2007: Linear and nonlinear signatures in the planetary wave dynamics of an AGCM: Probability density functions. *J. Atmos. Sci.*, **64**, 117–136, doi:10.1175/JAS3822.1.
- Branstator, G., 1983: Horizontal energy propagation in a barotropic atmosphere with meridional and zonal structure. *J. Atmos. Sci.*, **40**, 1689–1708, doi:10.1175/1520-0469(1983)040<1689:HEPIAB>2.0.CO;2.
- , 1990: Low-frequency patterns induced by stationary waves. *J. Climate*, **47**, 629–649, doi:10.1175/1520-0469(1990)047<0629:LFPIBS>2.0.CO;2.
- , 2002: Circumglobal teleconnections, the jet stream waveguide, and the North Atlantic Oscillation. *J. Climate*, **15**, 1893–1910, doi:10.1175/1520-0442(2002)015<1893:CTTJSW>2.0.CO;2.
- , and F. Selten, 2009: “Modes of variability” and climate change. *J. Climate*, **22**, 2639–2658, doi:10.1175/2008JCLI2517.1.
- Corti, S., F. Molteni, and T. N. Palmer, 1999: Signature of recent climate change in frequencies of natural atmospheric circulation regimes. *Nature*, **398**, 799–802, doi:10.1038/19745.

- Franzke, C., and S. B. Feldstein, 2005: The continuum and dynamics of Northern Hemisphere teleconnection patterns. *J. Climate*, **62**, 3250–3267, doi:10.1175/JAS3536.1.
- Hartmann, D. L., 2015: Pacific sea surface temperature and winter of 2014. *Geophys. Res. Lett.*, **42**, 1894–1902, doi:10.1002/2015GL063083.
- Hoerling, M. P., and A. Kumar, 2002: Atmospheric response patterns associated with tropical forcing. *J. Climate*, **15**, 2184–2203, doi:10.1175/1520-0442(2002)015<2184:ARPAWT>2.0.CO;2.
- Hoskins, B. J., and T. Ambrizzi, 1993: Rossby wave propagation on a realistic longitudinally varying flow. *J. Atmos. Sci.*, **50**, 1661–1671, doi:10.1175/1520-0469(1993)050<1661:RWPOAR>2.0.CO;2.
- Jong, B.-T., M. Ting, and R. Seager, 2016: El Niño impact on California precipitation: Seasonality, regionality, and El Niño intensity. *Environ. Res. Lett.*, **11**, 054021, doi:10.1088/1748-9326/11/5/054021.
- Kalnay, E., and Coauthors, 1996: The NCEP/NCAR 40-Year Reanalysis Project. *Bull. Amer. Meteor. Soc.*, **77**, 437–471, doi:10.1175/1520-0477(1996)077<0437:TNYRP>2.0.CO;2.
- Kay, J. E., and Coauthors, 2015: The Community Earth System Model (CESM) large ensemble project: A community resource for studying climate change in the presence of internal climate variability. *Bull. Amer. Meteor. Soc.*, **96**, 1333–1349, doi:10.1175/BAMS-D-13-00255.1.
- Lau, N.-C., 1981: A diagnostic study of recurrent meteorological anomalies appearing in a 15-year simulation with a GFDL general circulation model. *Mon. Wea. Rev.*, **109**, 2287–2311, doi:10.1175/1520-0493(1981)109<2287:ADSORM>2.0.CO;2.
- Lee, M., C. Hong, and H. Hsu, 2015: Compounding effects of warm sea surface temperature and reduced sea ice on the extreme circulation over the extratropical North Pacific and North America during the 2013–2014 boreal winter. *Geophys. Res. Lett.*, **42**, 1612–1618, doi:10.1002/2014GL062956.
- Linkin, M. E., and S. Nigam, 2008: The North Pacific Oscillation–west Pacific teleconnection pattern: Mature-phase structure and winter impacts. *J. Climate*, **21**, 1979–1997, doi:10.1175/2007JCLI2048.1.
- Madden, R. A., and P. R. Julian, 1971: Detection of a 40–50 day oscillation in the zonal wind in the tropical Pacific. *J. Atmos. Sci.*, **28**, 702–708, doi:10.1175/1520-0469(1971)028<0702:DOADOI>2.0.CO;2.
- North, G. R., T. L. Bell, R. F. Cahalan, and F. J. Moeng, 1982: Sampling errors in the estimation of empirical orthogonal functions. *Mon. Wea. Rev.*, **110**, 699–706, doi:10.1175/1520-0493(1982)110<0699:SEITEO>2.0.CO;2.
- Okumura, Y. M., and C. Deser, 2010: Asymmetry in the duration of El Niño and La Niña. *J. Climate*, **23**, 5826–5843, doi:10.1175/2010JCLI3592.1.
- Palmer, T. N., 2014: Record-breaking winters and global climate change. *Science*, **344**, 803–804, doi:10.1126/science.1255147.
- Rayner, N. A., D. E. Parker, E. B. Horton, C. K. Folland, L. V. Alexander, D. P. Rowell, E. C. Kent, and A. Kaplan, 2003: Global analyses of sea surface temperature, sea ice, and night marine air temperature since the late nineteenth century. *J. Geophys. Res.*, **108**, 4407, doi:10.1029/2002JD002670.
- Seager, R., and N. Henderson, 2016: Tropical ocean forcing of the persistent North American west coast ridge of winter 2013/14. *J. Climate*, **29**, 8027–8049, doi:10.1175/JCLI-D-16-0145.1.
- , M. Hoerling, S. Schubert, H. Wang, B. Lyon, A. Kumar, J. Nakamura, and N. Henderson, 2015: Causes of the 2011–14 California drought. *J. Climate*, **28**, 6997–7024, doi:10.1175/JCLI-D-14-00860.1.
- Swain, D., and Coauthors, 2014: The extraordinary California drought of 2013/2014: Character, context, and the role of climate change [in “Explaining Extreme Events of 2013”]. *Bull. Amer. Meteor. Soc.*, **95** (9), S3–S6.
- van Oldenborgh, G. J., R. Haarsma, H. De Vries, and M. R. Allen, 2015: Cold extremes in North America vs. mild weather in Europe: The winter of 2013–14 in the context of a warming world. *Bull. Amer. Meteor. Soc.*, **96**, 707–714, doi:10.1175/BAMS-D-14-00036.1.
- Wallace, J. M., and D. S. Gutzler, 1981: Teleconnections in the geopotential height field during the Northern Hemisphere winter. *Mon. Wea. Rev.*, **109**, 784–812, doi:10.1175/1520-0493(1981)109<0784:TITGHF>2.0.CO;2.
- Wang, S.-Y., L. Hipps, R. R. Gillies, and J.-H. Yoon, 2014: Probable causes of the abnormal ridge accompanying the 2013–2014 California drought: ENSO precursor and anthropogenic warming footprint. *Geophys. Res. Lett.*, **41**, 3220–3226, doi:10.1002/2014GL059748.
- Watson, P. A., A. Weisheimer, J. R. Knight, and T. N. Palmer, 2016: The role of the tropical west Pacific in the extreme Northern Hemisphere winter of 2013/2014. *J. Geophys. Res. Atmos.*, **121**, 1698–1714, doi:10.1002/2015JD024048.
- Williamson, D. L., 1983: Description of NCAR Community Climate Model (CCM0B). NCAR Tech. Note NCAR/TN-210+STR, 88 pp., doi:10.5065/D600002T.
- Yoon, J. H., S.-Y. Wang, R. R. Gillies, B. Kravitz, L. Hipps, and P. J. Rasch, 2015: Increasing water cycle extremes in California and in relation to ENSO cycle under global warming. *Nat. Commun.*, **6**, 8657, doi:10.1038/ncomms9657.
- Yu, B., and X. Zhang, 2015: A physical analysis of the severe 2013/2014 cold winter in North America. *J. Geophys. Res. Atmos.*, **120**, 10 149–10 165, doi:10.1002/2015JD023116.